Discontinuous boundary elements for steady-state fluid flow problems in discrete fracture networks

Discontinuous boundary elements for steady-state fluid flow problems in discrete fracture networks

Bin Wang[a], Yin Feng*[b], Xu Zhou[b], Sandra Pieraccini[c,f], Stefano Scialò[d,f], Corrado Fidelibus[e]

[a]*State Key Laboratory of Petroleum Resources and Prospecting, China University of Petroleum, Beijing 102249, China*
[b]*Department of Petroleum Engineering, University of Louisiana at Lafayette, Lafayette, Louisiana, USA*
[c]*Dipartimento di Ingegneria Meccanica e Aerospaziale, Politecnico di Torino, Torino, Italy*
[d]*Dipartimento di Scienze Matematiche, Politecnico di Torino, Torino, Italy*
[e]*Dipartimento di Ingegneria dell'Innovazione, Università del Salento, Lecce, Italy*
[f]*Member of INdAM-GNCS research group*

Abstract

Modeling fluid flow in three-dimensional (3D) Discrete Fracture Networks (DFNs) is of relevance in many engineering applications, such as oil/gas production, geothermal energy extraction, nuclear waste disposal and CO_2 sequestration. A new Boundary Element Method (BEM) technique with discontinuous quadratic elements, in conjunction with a parallel Domain Decomposition Method (DDM), is presented for the simulation of the steady-state fluid flow in DFNs, consisting of stochastically generated 3D planar fractures, arbitrarily oriented, and having differing hydraulic properties. Numerical examples characterized by DFNs of increasing complexity are proposed to show the accuracy and the efficiency of the presented technique, that provides good approximations of the fluid flow around domain interfaces, where the solution usually displays sharp gradients, like around intersections between traces (the segments originated by the intersection between two fractures), intersections between traces and fracture boundaries, or intersections between fractures and wellbores. The conjunction with a DDM approach is a promising strategy to speed up the computations, by also exploiting the advantages of parallel computing techniques. The technique is implemented in the code PyDFN3D, available at https://github.com/BinWang0213/PyDFN3D.

Keywords: Discrete Fracture Network (DFN), Fractured rock hydrology,

Boundary Element Method (BEM), Domain Decomposition Method (DDM), Subsurface fluid flow

1. Introduction

Modeling fluid flow in fractured rocks has been for a long of relevance in many engineering applications, such as oil/gas production, geothermal energy extraction, nuclear waste disposal and CO_2 sequestration [1, 2, 3, 4, 5, 6, 7]. Two predictive models are generally used: the Equivalent Porous Medium (EPM) and the Discrete Fracture Network (DFN). EPM is considered when fractures are highly connected and the fracture network can be condensed into a porous medium with an associated permeability tensor [8, 9]. The DFN model is an alternative to EPM models for multi-scale fracture networks, where all the fractures are explicitly represented [2, 10].

In the last decades, significant efforts have been made to simulate the fluid flow in three-dimensional (3D) DFNs and a variety of numerical approaches are now available. They can be categorized into: 1) mesh-based approaches, 2) Equivalent Pipe Networks (EPNs) and 3) Boundary Element Method (BEM) approaches.

In the mesh-based approaches, a computational mesh is generated over the entire fracture system and the flow field is then obtained by resorting to the Finite Element Method (FEM) or the Finite Volume Methods (FVM). Both methods offer considerable precision but, given the geometrical complexity of DFNs of practical interest, as, e.g. the one depicted in Fig.1a, for the use of high computational power and memory capacity may be required [11], especially for high-quality meshes and when a local grid refinement is applied to accurately resolve the sharp pressure gradients around fracture intersections (*traces*) or in the near-field of a well [10]. Even when the number of fractures in a DFN is relatively small, the number of mesh elements may be still considerable for conformity and quality constraints. A suitable mesh for FEM-based approaches is shown in Fig. 1b, for a DFN consisting of 932 fractures of various sizes and orientations. The mesh counts nearly 1.61 million nodes and 3.84 million triangular elements. To avoid the difficulties related to the mesh generation, non-conforming meshes, independently built on each fracture, are used, and the minimization of a cost functional is applied to enforce the coupling of a Domain Decomposition Method (DDM), resorting to error estimators to control the accuracy of the solution [12, 13, 14].

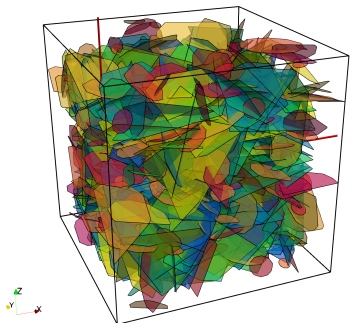

(a) A DFN with 932 fractures and several wellbores

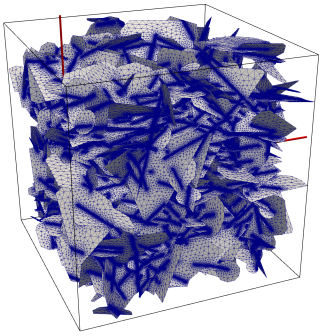

(b) FEM/FVM Mesh with 12.54 million 2D elements and 5.45 million nodes

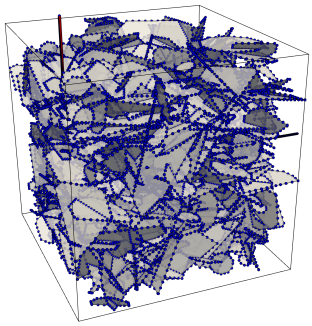

(c) BEM Mesh with 0.13 million 1D elements and 0.11 million nodes

Figure 1: A DFN example; comparison between FEM/FVM mesh and BEM mesh

Polygonal meshes are also suggested as an alternative to ease the generation of conforming meshes of complex DFNs, like in [15, 16, 17, 18], where the Virtual Element Method is used, in [19], where Mimetic Finite Differences (MFDs) and mixed finite elements are combined, and in [20], where Hybrid High Order (HHO) methods are applied.

In the EPN approach, a DFN is morphed into a network of one-dimensional conductors (*pipes*), endowed with an appropriate conductance value, and connecting the mid-points of the traces in a fracture [21, 22, 23, 24]. EPNs feature great advantages in terms of computational efficiency and simplicity and as such are suitable to model large fracture networks. However, unique pipe-connection patterns are difficult to generate and the equivalence gives rise to unavoidable errors. A graph-based method has been recently proposed to reduce the error of EPNs [25, 26, 27].

For the application of BEM approaches, a one-dimensional discretization of fracture edges and traces is required [28]; BEM reveals being very accurate to resolve sharp pressure gradients near traces and wellbores even when few one-dimensional elements are used. Semi-analytic basis functions are introduced for the representation of the variables [29, 30]. A suitable BEM mesh is shown in Fig. 1c for the same 932-fractures DFN, characterized by several boundary elements about two orders of magnitude less than the number of elements of the corresponding FEM mesh.

The literature related to the use of BEM for the prediction of the fluid flow in three-dimensional DFNs is still quite limited. Shapiro and Andersson [31, 28, 32] were the first to apply this method, by resorting to constant boundary elements for fracture edges and traces. Later, Lenti and Fidelibus [33] proposed an advanced BEM technique in which quadratic elements are used for fracture edges and constant elements for internal traces. The choice of constant elements is derived from the need to handle flux discontinuities at the intersections between two traces and between a trace and an edge in a fracture. An optimization procedure is also applied to reduce memory usage when solving the global matrix. The authors pointed out that the use of low-order constant elements may lead to up to 22% flux mismatch errors. Yang et al [34] and Chen et al [35, 36, 37, 38] recently proposed a BEM method to model transient shale gas flow problems in a 2D infinite domain where BEM with constant elements is used to solve matrix flow, whereas finite differences are used to solve 1D fracture flow, and the Laplace transform is used to resolve the transient flow.

Fast solutions for the flow regime are crucial for the industrial application of DFNs. In this respect, none of the three approaches mentioned above prevails in offering such solutions. However, the scientific community may benefit from any contribution to improving one of the methods. In this note, a new BEM technique is proposed for the prediction of the steady-state single-phase fluid flow in 3D DFNs. The novelty of the technique lies in the use of discontinuous quadratic basis functions for the boundary elements, in combination with a domain decomposition approach. Uniform permeability and aperture values are ascribed to each fracture. The fluid flow is governed by a two-dimensional Laplace equation, with sinks/sources located at the traces and at the intersections with wellbores (assumed linear). With the proposed technique, accurate predictions can be provided, also where large gradients are expected. Furthermore, with DDM, the way to the development of the technique for parallel solvers is paved, thus allowing the reduction of

the computational times.

The note is organized as follows: In Section 2, a detailed description of the adopted formulation and of the typical discretization associated with the proposed BEM technique is reported; in Section 3, the DDM algorithm is briefly introduced and commented; in Section 4, the technique is tested on three verification examples and one synthetic field application example; finally, the possible extensions of the technique are discussed and concluding remarks are drawn accordingly.

The technique is implemented in the computer code PyDFN3D.

2. BEM formulation

In this section, the BEM formulation adopted for the steady-state fluid flow in 3D DFNs is described. The derivation of the integral equations and of the final algebraic system is reported, given the special basis functions of the discontinuous elements.

The following assumptions are considered: 1) fluid dynamic properties are constant and independent of the pressure; 2) the rock matrix is impervious, such that the fluid flow occurs only inside fractures, through fracture intersections and in wellbores; 3) fracture aperture and permeability are uniforms within each fracture but different values are allowed among different fractures; 4) the gravity effects are ignored, implicitly assuming that the thickness of the fractured reservoir is small compared with the horizontal extension [39, 40]; however, the formulation can be easily extended to include such effects; 5) pressure drops caused by friction in wellbores are neglected, thus pressure inside is uniform.

2.1. Boundary integral equations

With reference to a coordinate system $\mathbf{X}=\{X_1, X_2, X_3\}$, arbitrarily oriented in the 3D space, a plane π is considered. The unit vector normal to π is $\mathbf{n}_\pi$. A local reference system $\mathbf{x} = \{x_1, x_2\}$ is chosen on π. A domain $\Omega \subset \pi$ is introduced; the boundary of Ω is denoted by Γ and $\mathbf{n}$ is the unit normal vector to Γ, outward-pointing from Ω. A 3D fracture $\Omega^\star$ is defined such that $\Omega^*=\{X:X=\gamma+b_\mathrm{f}\mathbf{t}_\pi, \gamma \in \pi\}$, being $b_\mathrm{f}(\mathbf{x})$ the fracture aperture, a number much smaller than each dimension of Ω in π. For the above-mentioned hypotheses, fracture aperture $b_\mathrm{f}(\mathbf{x})=b_\mathrm{f}$ is uniform in π and the top and bottom walls of the fracture are planes parallel to π. The fluid velocity vectors inside the fracture are all parallel to π.

Given the fracture intrinsic permeability k (unit m^2) uniform in $\Omega^\star$, the fluid dynamic viscosity μ (unit kg $\mathrm{m}^{-1}\mathrm{s}^{-1}$) independent of the pressure p, and by neglecting, as mentioned, the gravity effects, the governing equation for the steady-state fluid flow in $\Omega^\star$ with a generic volumetric source term $Q(\mathbf{X})$ (unit s^{-1}) can be expressed as follows [41]:

$$-\frac{k}{\mu}\nabla^2 p(\mathbf{X}) = Q(\mathbf{X}) \tag{1}$$

where $p(\mathbf{X})$ is the fluid pressure (unit kg $\mathrm{m}^{-1}\mathrm{s}^{-2}$). The 3D problem can be reduced into a 2D problem by averaging Eq.(1) along $\mathbf{n}_\pi$. By splitting the operator ∇ in an in-plane component ∇_π and a normal component $\nabla_{\mathbf{n}_\pi}$, one has:

$$-\frac{k}{\mu}\nabla_\pi^2 \int_{(-b_\mathrm{f}/2)}^{(b_\mathrm{f}/2)} p(\mathbf{X})\mathrm{d}\mathbf{n}_\pi = \int_{(-b_\mathrm{f}/2)}^{(b_\mathrm{f}/2)} Q(\mathbf{X})\mathrm{d}\mathbf{n}_\pi - \frac{k b_\mathrm{f}}{\mu}\nabla_\pi^2 \tilde{p}(\mathbf{x}) = q(\mathbf{x}) \tag{2}$$

in which $\tilde{p}(\mathbf{x}){=}\frac{1}{b_\mathrm{f}}\int_{(-b_\mathrm{f}/2)}^{(b_\mathrm{f}/2)} p(\mathbf{X})\mathrm{d}\mathbf{n}_\pi$ is the averaged pressure along $\mathbf{n}_\pi$, tech $q(\mathbf{x}){=}\frac{1}{b_\mathrm{f}}\int_{(-b_\mathrm{f}/2)}^{(b_\mathrm{f}/2)} Q(\mathbf{X})\mathrm{d}\mathbf{n}_\pi$ is a distributed areal source. In what follows, the fracture is dimensionally reduced to the planar domain coinciding with Ω, ∇ is used for ∇_π and p is assimilated to $\tilde{p}$.

The fractures of a DFN can mutually intercept, therefore, for the reduction to planes, the intersections are segments (*traces*). Also wellbores can cross the fractures, and the intersections are point intersections (*wellbore intersections*).

As the rock matrix is impervious, there is no leakage from the blocks bounded by the fractures, and therefore there are no areal sources; rather the source term $q(\mathbf{x})$ is given by linear sources and point sources [41] from the traces and the wellbore intersections, respectively. Traces in Ω are labeled by t, whereas T is the set of all the traces in the same domain; wellbore intersections are denoted by s, and S denotes the set of all the wellbore intersections in Ω, therefore, the source term $q(\mathbf{x})$ can be written as:

$$q(\mathbf{x}) = \sum_{t\in T} \delta_{t,q_t} + \sum_{s\in S} q_s \delta_s \tag{3}$$

being δ_{t,q_t} the Dirac Delta function defined, for any sufficiently regular function $\varphi(\mathbf{x})$, as $\langle \delta_{t,q_t}, \varphi\rangle {=} \int_t q_t(\gamma)\varphi(\gamma)\mathrm{d}\gamma$, where $q_t(\gamma)$ (unit $\mathrm{m}^2\mathrm{s}^{-1}$) is the concentrated volumetric source per unit trace length on t, whereas δ_s, for a

wellbore $s \in S$, is the Dirac Delta function located at the intersection point $\mathbf{x}_s$ between the well and the mean fracture plane, defined by $\langle \delta_s, \varphi \rangle = \varphi(\mathbf{x}_s)$, and q_s (unit $\mathrm{m^3 s^{-1}}$) is the volumetric point source at wellbore s.

By substituting Eq. (3) into Eq. (2), the governing equation for the fluid flow in a fracture is obtained as [42]:

$$-\frac{kb_\mathrm{f}}{\mu}\nabla^2 p = \sum_{t\in T}\delta_{t,q_t} + \sum_{s\in S} q_s \delta_s \tag{4}$$

After adding Dirichlet and Neumann boundary conditions, a Boundary Integral Equation (BIE) corresponding to Eq. (4) is obtained in each collocation point $\mathbf{x}_i \in \bar{\Omega}$:

$$\begin{aligned} -\frac{kb_\mathrm{f}}{\mu}\left[c(\mathbf{x}_i)p(\mathbf{x}_i) + \int_\Gamma p(\mathbf{x})\frac{\partial w(\mathbf{x}_i,\mathbf{x})}{\partial \mathbf{n}}\mathrm{d}\Gamma\right] = \\ -\frac{kb_\mathrm{f}}{\mu}\int_\Gamma \frac{\partial p}{\partial \mathbf{n}}(\mathbf{x}) w(\mathbf{x}_i,\mathbf{x})\mathrm{d}\Gamma \\ -\sum_{t\in T}\int_t q_t(\mathbf{x}) w(\mathbf{x}_i,\mathbf{x})\mathrm{d}t - \sum_{s\in S} q_s w(\mathbf{x}_i,\mathbf{x}_s) \end{aligned} \tag{5}$$

where $\partial p/\partial \mathbf{n}$ is the directional derivative of p along the normal, and w, $\partial w/\partial \mathbf{n}$ are a weighing function and its normal derivative, respectively. The quantity $c(\mathbf{x}_i)$ is a number depending on the location of $\mathbf{x}_i$; namely, if it is in the interior or on the boundary of the domain. The definition of weighing functions is given in the following.

By neglecting the gravity, the fluid velocity $\mathbf{u}$ (unit $\mathrm{ms^{-1}}$) is equal to -$(k/\mu)\nabla p$; the corresponding BIE for the components $u_j(\mathbf{x}_i)$ is:

$$\begin{aligned} c(\mathbf{x}_i)u_j(\mathbf{x}_i)b_\mathrm{f} - \frac{kb_\mathrm{f}}{\mu}\int_\Gamma p(\mathbf{x})\frac{\partial}{\partial x_j}\left[\frac{\partial w(\mathbf{x}_i,\mathbf{x})}{\partial \mathbf{n}}\right]\mathrm{d}\Gamma \\ = -\frac{kb_\mathrm{f}}{\mu}\int_\Gamma \frac{\partial p}{\partial \mathbf{n}}(\mathbf{x})\frac{\partial w(\mathbf{x}_i,\mathbf{x})}{\partial x_j}\mathrm{d}\Gamma \\ -\sum_{t\in T}\int_t q_t(\mathbf{x})\frac{\partial w(\mathbf{x}_i,\mathbf{x})}{\partial x_j}\mathrm{d}t - \sum_{s\in S} q_s \frac{\partial w(\mathbf{x}_i,\mathbf{x}_s)}{\partial x_j} \end{aligned} \tag{6}$$

Details on derivation and notation for the above BIEs are given in Appendix A. The weighting function w corresponds to the fundamental solution

of the steady-state fluid flow equation for a source point $\mathbf{x}_i$. The function w and the derivative $\partial w/\partial \mathbf{n}$ with respect to the normal $\mathbf{n}$ are [43]:

$$\begin{aligned} w(\mathbf{x}_i, \mathbf{x}) &= \frac{1}{2\pi} \ln \frac{1}{r(\mathbf{x}_i, \mathbf{x})} \\ \frac{\partial w(\mathbf{x}_i, \mathbf{x})}{\partial \mathbf{n}} &= \frac{1}{2\pi} \frac{(\mathbf{x}_i - \mathbf{x}) \cdot \mathbf{n}}{r^2(\mathbf{x}_i, \mathbf{x})} \end{aligned} \tag{7}$$

where $r(\mathbf{x}_i, \mathbf{x})$ is the distance between $\mathbf{x}_i$ and $\mathbf{x}$.

2.2. Discretization with discontinuous quadratic elements

Lenti and Fidelibus [33] proposed a BEM technique for DFNs in which constant basis functions for the traces were used to deal with the flux discontinuities at trace-trace and trace-boundary intersections. However, due to the low accuracy of the constant element approximation, the application of the technique implies errors increasing with the geometrical complexity of the DFN. In this note, an advancement is proposed by resorting to quadratic basis functions and discontinuous Boundary Elements (BEs), intrinsically including flux discontinuities at the nodes. As shown in Fig. 2, the dis-

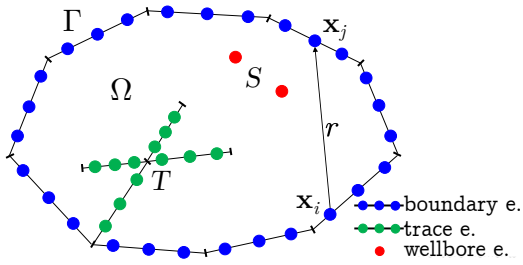

Figure 2: BEM discretization for a fracture domain; $\mathbf{x}_i$ is a collocation node, $\mathbf{x}_j$ an integration node; blue, green and red dots represent the nodes for the boundary elements, the trace elements and the wellbore elements, respectively

cretization of each fracture is obtained by subdividing the boundary Γ and the traces $t \in T$ in straight BEs. Collocation nodes are then placed on each element. Three collocation nodes are placed on each BE, to uniquely identify a quadratic polynomial on each element; three quadratic basis functions $N_i(\mathbf{x})$, i=1, ..., 3 are consequently defined on each BE by the condition $N_i(\mathbf{x}_j)$=δ_{ij}, for i, j=1, ..., 3, being δ_{ij} the Kronecker delta. The basis functions related to each BE are then extended to zero outside the element.

Additional nodes are also placed at wellbore intersections $s \in S$. It is worth noting that collocation nodes never coincide with trace-trace intersections and trace-boundary intersections, where the flux of p is discontinuous. This is achieved by ensuring that trace intersection points and trace-boundary intersection points coincide with BE endpoints, whereas collocation nodes are placed in the interior of each element, as shown in Fig. 2, where collocation points are shown in blue, green or red spots.

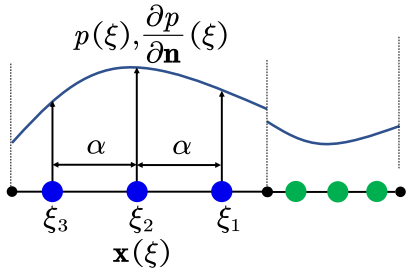

Figure 3: Discontinuous quadratic element used for boundary and trace elements, with $-1 \leqslant \xi \leqslant 1$, $\xi_1 = -\alpha, \xi_2 = 0, \xi_3 = \alpha$.

The set of elemental basis functions is denoted by $\mathbf{N}=\{N_i\}_{i=1,\dots,3}$ and the approximation of the pressure p and of its normal derivative are:

$$p(\xi) = \sum_{i=1}^{3} p_i N_i(\xi), \quad \frac{\partial p}{\partial \mathbf{n}}(\xi) = \sum_{i=1}^{3} (\frac{\partial p}{\partial \mathbf{n}})_i N_i(\xi), \quad -1 \leqslant \xi \leqslant 1 \tag{8}$$

where ξ is a local normalized coordinate, and p_i, $(\partial p/\partial \mathbf{n})_i$ are nodal values. Functions in $\mathbf{N}$ are defined as follows:

$$N_1 = \frac{1}{2}\frac{\xi}{\alpha}\left(\frac{\xi}{\alpha} - 1\right), \quad N_2 = \left(1 - \frac{\xi}{\alpha}\right)\left(1 + \frac{\xi}{\alpha}\right), \quad N_3 = \frac{1}{2}\frac{\xi}{\alpha}\left(\frac{\xi}{\alpha} + 1\right) \tag{9}$$

with $0 < \alpha \leq 1$, and α is a collocation factor. Choosing $0 < \alpha < 1$, the first and the third node on each element are shifted inside it by a normalized quantity equal to α. A value α=0.67 is used here, as suggested in [44]. Boundaries and traces are approximated by using the same functions in $\mathbf{N}$, using $\mathbf{x}=\sum_{i=1}^{3} \mathbf{x}_i N_i(\xi)|_{\alpha=1}$, i.e. the shape functions of Eq. (9) with α=1.

A global numbering can be introduced for the collocation nodes and for the basis functions on all the BEs, and J_{tot} is defined as the set of the indexes of all the nodes in the discretization. The following subsets of J_{tot}

are also introduced: J_Γ, containing the indexes of the nodes belonging to the boundary Γ; J_t, containing the indexes of the nodes belonging to trace $t \in T$; J_s, containing the index of the node matching $\mathbf{x}_s$, and $J_T = \bigcup_{t\in T} J_t$, $J_S = \bigcup_{s\in S} J_s$. Without loss of generality, the indexes of these sets are numbered consecutively, starting from J_Γ, continuing with J_T and ending with J_S.

In what follows

$$p^\Gamma(\mathbf{x}) = \sum_{j\in J_\Gamma} p_j^\Gamma N_j(\mathbf{x}), \quad p^T(\mathbf{x}) = \sum_{j\in J_T} p_j^T N_j(\mathbf{x}), \quad p^S(\mathbf{x}) = \sum_{j\in J_S} p_j^S N_j(\mathbf{x})$$

denote the discrete solution on Γ, on the traces and on the wellbore intersections, respectively. Similarly, the discrete counterpart of $\partial p/\partial \mathbf{n}$ on Γ is defined by

$$\left(\frac{\partial p}{\partial \mathbf{n}}\right)^\Gamma(\mathbf{x}) = \sum_{j\in J_\Gamma} \left(\frac{\partial p}{\partial \mathbf{n}}\right)_j^\Gamma N_j(\mathbf{x}),$$

whereas the source on trace $t \in T$ is denoted by $q_t^t(\mathbf{x})=\sum_{j\in J_t} q_j^t N_j(\mathbf{x})$. Finally, $\mathbf{p}^\star$, $\star \in \{\Gamma, T, S\}$ is the array collecting column-wise the unknowns $\mathbf{p}_j^\star$, $j \in J_\star$, $(\partial\mathbf{p}/\partial\mathbf{n})^\Gamma$ the array collecting the unknowns $(\partial p/\partial\mathbf{n})_j^\Gamma$, $j \in J_\Gamma$, whereas $\mathbf{q}^T$ collects the coefficients q_j^t, for $j \in J_t$ and $t \in T$, and $\mathbf{q}^S$ collects the coefficients q_s, $s \in S$.

The use of above definitions into the BIE Eq. (5) yields:

$$\begin{aligned}
\mathbf{C}^\Gamma\mathbf{p}^\Gamma + \mathbf{H}^{\Gamma\Gamma}\mathbf{p}^\Gamma &= \mathbf{G}^{\Gamma\Gamma}\left(\frac{\partial\mathbf{p}}{\partial\mathbf{n}}\right)^\Gamma + \mathbf{G}^{\Gamma T}\mathbf{q}^T + \mathbf{G}^{\Gamma S}\mathbf{q}^S \\
\mathbf{C}^T\mathbf{p}^T + \mathbf{H}^{T\Gamma}\mathbf{p}^\Gamma &= \mathbf{G}^{T\Gamma}\left(\frac{\partial\mathbf{p}}{\partial\mathbf{n}}\right)^\Gamma + \mathbf{G}^{TT}\mathbf{q}^T + \mathbf{G}^{TS}\mathbf{q}^S \\
\mathbf{C}^S\mathbf{p}^S + \mathbf{H}^{S\Gamma}\mathbf{p}^\Gamma &= \mathbf{G}^{S\Gamma}\left(\frac{\partial\mathbf{p}}{\partial\mathbf{n}}\right)^\Gamma + \mathbf{G}^{ST}\mathbf{q}^T + \mathbf{G}^{SS}\mathbf{q}^S
\end{aligned} \tag{10}$$

where $\mathbf{C}^\star$, $\star \in \{\Gamma, T, S\}$, are matrices with diagonal entries $\mathbf{C}_{ii}^\star$ equal to $(kb_\mathrm{f})/\mu$ when $\mathbf{x}_i$ is in the interior of the domain Ω, and equal to $(kb_\mathrm{f})/(2\mu)$ when $\mathbf{x}_i$ is on the boundary; the G-type and H-type matrices are defined as

follows:

$$
\begin{aligned}
G_{ij}^{\Gamma\Gamma} &= \frac{kb_{\mathrm{f}}}{\mu}\int_{\Gamma} w(\mathbf{x}_i,\mathbf{x})N_j(\mathbf{x})\mathrm{d}\Gamma, \quad i,j\in J_\Gamma;\\
G_{ij}^{\Gamma T} &= \int_{t} w(\mathbf{x}_i,\mathbf{x})N_j(\mathbf{x})\mathrm{d}t, \quad i\in J_\Gamma, j\in J_t, t\in T;\\
G_{ij}^{\Gamma S} &= w(\mathbf{x}_i,\mathbf{x})N_j(\mathbf{x}), \quad i\in J_\Gamma, j\in J_S;\\
G_{ij}^{T\Gamma} &= \frac{kb_{\mathrm{f}}}{\mu}\int_{\Gamma} w(\mathbf{x}_i,\mathbf{x})N_j(\mathbf{x})\mathrm{d}\Gamma, \quad i\in J_t, j\in J_\Gamma, t\in T\\
G_{ij}^{TT} &= \int_{t} w(\mathbf{x}_i,\mathbf{x})N_j(\mathbf{x})\mathrm{d}t, \quad i,j\in J_t, t\in T;\\
G_{ij}^{TS} &= w(\mathbf{x}_i,\mathbf{x})N_j(\mathbf{x}), \quad i\in J_T, j\in J_S;\\
G_{ij}^{S\Gamma} &= \frac{kb_{\mathrm{f}}}{\mu}\int_{\Gamma} w(\mathbf{x}_i,\mathbf{x})N_j(\mathbf{x})\mathrm{d}\Gamma, \quad i\in J_S, j\in J_\Gamma;\\
G_{ij}^{ST} &= \int_{t} w(\mathbf{x}_i,\mathbf{x})N_j(\mathbf{x})\mathrm{d}t, \quad i\in J_S, j\in J_T;\\
G_{ii}^{SS} &= \frac{1}{2\pi}\ln r_i, \quad i\in J_S;\\
G_{ij}^{SS} &= w(\mathbf{x}_i,\mathbf{x}), \quad i\neq j\in J_S;\\
H_{ij}^{\Gamma\Gamma} &= \frac{kb_{\mathrm{f}}}{\mu}\int_{\Gamma} \frac{\partial w}{\partial \mathbf{n}}(\mathbf{x}_i,\mathbf{x})N_j(\mathbf{x})\mathrm{d}\Gamma, \quad i,j\in J_\Gamma;\\
H_{ij}^{S\Gamma} &= \frac{kb_{\mathrm{f}}}{\mu}\int_{\Gamma} \frac{\partial w}{\partial \mathbf{n}}(\mathbf{x}_i,\mathbf{x})N_j(\mathbf{x})\mathrm{d}\Gamma, \quad i\in J_S, j\in J_\Gamma;\\
H_{ij}^{T\Gamma} &= \frac{kb_{\mathrm{f}}}{\mu}\int_{\Gamma} \frac{\partial w}{\partial \mathbf{n}}(\mathbf{x}_i,\mathbf{x})N_j(\mathbf{x})\mathrm{d}\Gamma, \quad i\in J_t, j\in J_\Gamma, t\in T
\end{aligned}
\tag{11}
$$

Note that in general $G^{T\Gamma}\neq\left(G^{\Gamma T}\right)^{\intercal}$, $G^{ST}\neq\left(G^{TS}\right)^{\intercal}$, $G^{S\Gamma}\neq\left(G^{\Gamma S}\right)^{\intercal}$. The diagonal entries of G^{SS} go to infinity as the distance $r(\mathbf{x}_i,\mathbf{x})$ approaches zero. To handle the singularity and apply the constant pressure boundary condition at a wellbore, nodes of unknown pressure $p^S(\mathbf{x})$ are placed on the boundaries, at distance r_s from the wellbore center, where the node is located. This handling of the wellbores was used and validated in a previous work [30].

Eq. (10) can be expressed in compact form as follows:

$$
\begin{bmatrix} \mathbf{C}^{\Gamma}+\mathbf{H}^{\Gamma\Gamma} & \mathbf{0} & \mathbf{0} \\ \mathbf{H}^{T\Gamma} & \mathbf{C}^{T} & \mathbf{0} \\ \mathbf{H}^{S\Gamma} & \mathbf{0} & \mathbf{C}^{S} \end{bmatrix} \begin{Bmatrix} \mathbf{p}^{\Gamma} \\ \mathbf{p}^{T} \\ \mathbf{p}^{S} \end{Bmatrix} = \begin{bmatrix} \mathbf{G}^{\Gamma\Gamma} & \mathbf{G}^{\Gamma T} & \mathbf{G}^{\Gamma S} \\ \mathbf{G}^{T\Gamma} & \mathbf{G}^{TT} & \mathbf{G}^{TS} \\ \mathbf{G}^{S\Gamma} & \mathbf{G}^{ST} & \mathbf{G}^{SS} \end{bmatrix} \begin{Bmatrix} \left(\frac{\partial \mathbf{p}}{\partial \mathbf{n}}\right)^{\Gamma} \\ \mathbf{q}^{T} \\ \mathbf{q}^{S} \end{Bmatrix} \tag{12}
$$

On each node of the boundary, either pressure p or flux $\partial p/\partial n$ can be specified, corresponding to a Dirichlet or a Neumann condition, respectively. Thus, the columns of the matrices in Eq. (12) can be re-ordered to have the coefficients of all the unknowns on the left-hand side and the coefficients of all the known terms on the right-hand side. However, the prevailing condition is the insulation condition, i.e. $\partial p/\partial n$=0. Once the solution of Eq. (12) is obtained, pressure and velocity at any point $\mathbf{x}_i$ can be calculated by applying Eqs. (5)-(6).

In this work, a simple wellbore model is considered that assumes a wellbore has a low production/injection rate, large pipe diameter and short segment length in the gravitational direction. Thus, the pressure along the wellbore is assumed to be constant.[45] For a wellbore with a flow rate q_w intersecting multiple fracture planes in $s_1, s_2, \ldots, s_n$ intersection points, each one on a different fracture, one additional condition need to be added to the system (12). Given q_{s_i}, the flow rate at intersection s_i, the equation $\sum_{i=1}^{n} q_{s_i}$=q_w is added, which together with the assumption of constant pressure in the well is sufficient to close the problem.

2.3. Fast analytical BIE integration

After the BEM discretization is performed, given the singularity of the fundamental solution w, there is the need to perform singular integrations, nearly-singular integrations and non-singular integrations. The singular and nearly-singular integrations require special techniques to avoid the loss of accuracy related to standard numerical integration [29]. Element subdivision, analytical and semi-analytical integration, adaptive Gaussian quadrature, coordinate transformation and BIE modification [46, 47, 48] can be adopted. Exact analytical integration formulations are also available [44, 49, 50]. In this note, an exact integration formulation for discontinuous quadratic elements is derived based on the method proposed in [49]. The expressions for the integrals of G-type and H-type matrices for a boundary or a trace integration element in Eq. (11) are reported in what follows (the quantities $A_l, D_l, E_l, F_l, I_l, S_l, T_l$ $(l = 0, \ldots, 2)$ and a, e are defined in Appendix B):

$$\begin{aligned} \int_{\star} w(\mathbf{x}_i, \mathbf{x}) N_j(\mathbf{x}) \mathrm{d}\star &= [G_1, G_2, G_3]^T \\ \int_{\star} \frac{\partial w(\mathbf{x}_i, \mathbf{x})}{\partial \mathbf{n}} N_j(\mathbf{x}) \mathrm{d}\star &= [H_1, H_2, H_3]^T \end{aligned} \qquad \star \in \{\Gamma, T\} \tag{13}$$

When a collocation node does not pertain to the integration element, the analytical integration formulations are:

$$\begin{gathered} G_1 = \frac{J}{8\pi}\left(\frac{A_2}{\alpha^2} - \frac{A_1}{\alpha}\right), G_2 = \frac{J}{4\pi}\left(A_0 - \frac{A_2}{\alpha^2}\right), G_3 = \frac{J}{8\pi}\left(\frac{A_2}{\alpha^2} + \frac{A_1}{\alpha}\right) \\ H_1 = \frac{e}{4\pi}\left(\frac{F_2}{\alpha^2} - \frac{F_1}{\alpha}\right), H_2 = \frac{e}{2\pi}\left(F_0 - \frac{F_2}{\alpha^2}\right), H_3 = \frac{e}{4\pi}\left(\frac{F_2}{\alpha^2} + \frac{F_1}{\alpha}\right) \end{gathered} \tag{14}$$

where J is the Jacobian of the map from physical to reference element given by Eq. (B.1). When a collocation node is instead on the integration element, the formulations are:

$$\begin{gathered} G_1 = \frac{J}{4\pi}\left(\frac{S_2}{\alpha^2} - \frac{S_1}{\alpha}\right), G_2 = \frac{J}{2\pi}\left(S_0 - \frac{S_2}{\alpha^2}\right), G_3 = \frac{J}{4\pi}\left(\frac{S_2}{\alpha^2} + \frac{S_1}{\alpha}\right) \\ H_1 = H_2 = H_3 = 0 \end{gathered} \tag{15}$$

For the discretized form of Eq. (6), the derivatives with respect to x_k ($k = 1, 2$) of the terms of the G-type and H-type matrices are required and are as follows:

$$\begin{gathered} \int_\star \frac{\partial w(\mathbf{x}_i, \mathbf{x})}{\partial x_k} N_j(\mathbf{x}) \mathrm{d}\star = \left[\frac{\partial G_1}{\partial x_k}, \frac{\partial G_2}{\partial x_k}, \frac{\partial G_3}{\partial x_k}\right]^T \\ \int_\star \frac{\partial}{\partial x_k}\left[\frac{\partial w(\mathbf{x}_i, \mathbf{x})}{\partial \mathbf{n}}\right] N_j(\mathbf{x}) \mathrm{d}\star = \left[\frac{\partial H_1}{\partial x_k}, \frac{\partial H_1}{\partial x_k}, \frac{\partial H_1}{\partial x_k}\right]^T \end{gathered} \quad \star = \{\Gamma, T\} \tag{16}$$

Again, when a collocation node does not pertain to the integration element, the formulations are:

$$\begin{gathered} \frac{\partial G_1}{\partial x_k} = -\frac{J}{4\pi}\left(\frac{E_{k2}}{a^2} - \frac{E_{k1}}{a}\right), \quad \frac{\partial G_2}{\partial x_k} = -\frac{J}{4\pi}\left(E_{k0} - \frac{E_{k2}}{a^2}\right) \\ \frac{\partial G_3}{\partial x_k} = -\frac{J}{4\pi}\left(\frac{E_{k2}}{a^2} + \frac{E_{k1}}{a}\right), \frac{\partial H_1}{\partial x_k} = \frac{1}{4\pi}\left(\frac{I_{k2}}{a^2} - \frac{I_{k1}}{a}\right) \\ \frac{\partial H_2}{\partial x_k} = \frac{1}{4\pi}\left(I_{k0} - \frac{I_{k2}}{a^2}\right), \quad \frac{\partial H_3}{\partial x_k} = \frac{1}{4\pi}\left(\frac{I_{k2}}{a^2} + \frac{I_{k1}}{a}\right) \end{gathered} \tag{17}$$

Finally, when a collocation node is on the integration element, the formulations are:

$$\begin{gathered} \frac{\partial G_1}{\partial x_k} = \frac{JD_k}{4\pi\alpha}\left(\frac{T_2}{\alpha^2} - \frac{T_1}{\alpha}\right), \frac{\partial G_2}{\partial x_k} = \frac{JD_k}{2\pi\alpha}\left(T_0 - \frac{T_2}{\alpha^2}\right), \frac{\partial G_3}{\partial x_k} = \frac{JD_k}{4\pi\alpha}\left(\frac{T_2}{\alpha^2} + \frac{T_1}{\alpha}\right) \\ \frac{\partial H_1}{\partial x_k} = \frac{\partial H_2}{\partial x_k} = \frac{\partial H_3}{\partial x_k} = 0 \end{gathered} \tag{18}$$

As previously mentioned, all the formulations above are implemented and tested in the computer code PyDFN3D.

3. Parallel domain decomposition method

For large DFN problems, in the context of BEM, the direct coupling, i.e. the assembly of a large system of equations, including the compatibility conditions at the interfaces among adjacent domains, may too computationally demanding. In previous works, parallel DDMs were developed aimed at iteratively solving a series of small dense linear subsystems, rather than a coupled large unsymmetrical sparse linear system [51, 52, 53, 54]. In DDM, conditions at interfaces are updated at each iteration, until a solution that fits the specified compatibility condition at each interface is obtained. Here the main idea behind a DDM strategy suitable for the proposed approach is recalled, referring to [54] and to references therein for a deeper analysis on such methods.

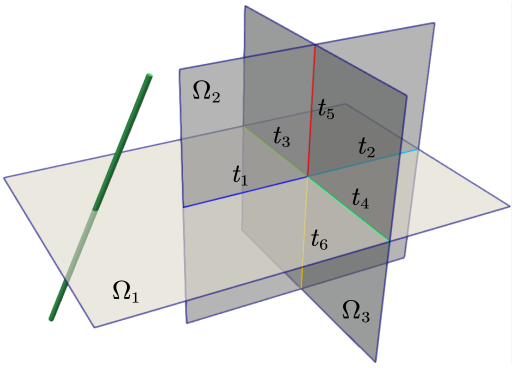

Figure 4: A DFN with 3 fracture planes $(\Omega_1, \Omega_2, \Omega_3)$ and six intersection traces $(t_1, t_2, t_3, t_4, t_5, t_6)$.

A network of N_F fractures Ω_k and N_T traces is considered, like the one in Fig. 4, being the set of all traces on fracture Ω_k denoted by T_k, k=1, ..., N_F, and the set of all the traces in the network denoted by $\mathcal{T}$. Each trace $t \in \mathcal{T}$ is shared by exactly two fractures Ω_I and Ω_J, $I \neq J \in [1, \ldots, N_F]$, such that a map τ between each trace and the corresponding pair of fracture indexes can be introduced: $\tau(t) = \{I, J\}$, being $t = \bar{\Omega}_I \cap \bar{\Omega}_J$.

Compatibility conditions at the traces are the continuity of pressure and

the balance of normal fluxes, which can be expressed as follows:

$$\begin{array}{c} \mathbf{q}_{I,t} + \mathbf{q}_{J,t} = 0 \\ \mathbf{p}_{I,t} = \mathbf{p}_{I,t} \end{array} \quad \text{on } t,\ \{I,J\} = \tau(t) \tag{19}$$

where $q_{I,t}$, $p_{I,t}$ are the restriction of quantities q_I and p_I, respectively, to trace t on fracture Ω_I, for $t \in T_I$. Then, the parallel domain decomposition algorithm here used for the resolution of large DFN problems is depicted in Table 1, in which the superscript is used to indicate the iteration counter.

Table 1: Parallel domain decomposition algorithm

---

1. set k=0 and initial guess $\mathbf{p}^0_{I,t}$ on each fracture Ω_I, $I = 1, \ldots, N_F$ at each intersection trace, $t \in T_I$
2. compute $\mathbf{q}^0_I$ by solving Eq. (10) on each fracture domain Ω_I, I = 1,...,N_F

while $\varepsilon = \sum_{I=1}^{N_F} \sum_{t \in T_I} \|\mathbf{p}^{k+1}_{I,t} - \mathbf{p}^k_{I,t}\| / \|\mathbf{p}^k_{I,t}\| <$ TOL **do**

3. update $\mathbf{p}^{k+1}_{I,t} = \mathbf{p}^k_{I,t} - \beta^k \left(\mathbf{q}^k_{I,t} + \mathbf{q}^k_{J,t}\right)$, at each intersection trace $t \in \mathcal{T}$, $\{I,J\} = \tau(t)$
4. compute $\mathbf{q}^{k+1}_{I,t}$ by solving Eq. (10) at each sub-domain Ω_I, I = 1,...,N_F, $t \in T_I$
5. k=k+1

end while

It is to remark that, according to the solution strategy, the compatibility conditions of Eq. (19) are satisfied up to a given tolerance TOL, this quantity being directly associated with the mass flux balance over all intersections. The optimal relaxation parameter β^k is defined as follows [54]:

$$\beta^k = \frac{\sum_{t \in \mathcal{T}} \boldsymbol{\epsilon}^k_{p,I,t} \cdot (\boldsymbol{\epsilon}^k_{q,I,t} + \boldsymbol{\epsilon}^k_{q,J,t})}{\sum_{t \in \mathcal{T}} \|\boldsymbol{\epsilon}^k_{q,I,t} + \boldsymbol{\epsilon}^k_{q,J,t}\|^2}, \quad \{I,J\} = \tau(t) \tag{20}$$

with error terms between two iterations $\boldsymbol{\epsilon}^k_{p,I,t}$=$\mathbf{p}^{k+1}_{I,t} - \mathbf{p}^k_{I,t}$, and $\boldsymbol{\epsilon}^k_{q,I,t}$=$\mathbf{q}^{k+1}_{I,T_K} - \mathbf{q}^k_{I,t}$. Clearly, lower values of TOL yield better flux balance at the traces, at the cost of a larger number of iterations and computational time. A TOL value of $1 \times 10^{-6} - 1 \times 10^{-9}$ is used for the following computations.

4. Numerical examples

In this section, four numerical examples (Tests 1-4) for the validation of the proposed numerical technique are illustrated: the first example refers to a problem with a known exact solution, the second one is a test on a single fracture with multiple traces and one wellbore intersection, examples 3-4 are aimed at demonstrating the robustness and the reliability of the technique when dealing with more complex DFN systems. The DFN for the last example is stochastically generated by drawing position, orientation, size and permeability of each fracture from given Probability Density Functions (PDFs), as practice for DFNs, using the open-source DFN generator ADFNE [55]. Detailed information for all the examples below is available associated with the source code PyDFN3D.

4.1. Test 1: unit square problem

Consider a Darcy problem in a unit square domain Ω=$\{(x, y) \in (0,1) \times (0,1)\}$ with μ=1, k=1 and b_{f}=1 (see Fig. 5). The following boundary conditions are prescribed (see Fig. 5):

$$p\,(x, y) = 15\cos(4\pi x)\frac{\sinh\,(4\pi y)}{\pi\cosh(4\pi)} \tag{21}$$

Error indicators are considered in what follows to evaluate and compare the accuracy of the proposed technique, defined as:

$$\begin{aligned} e_p &= \sqrt{\frac{\sum_{l=1}^{N} t(p_{l,\mathrm{exact}} - p_{l,h})^2}{N}} \\ e_{\mathbf{u}} &= \sqrt{\frac{\sum_{l=1}^{N} (\mathbf{u}_{l,\mathrm{exact}} - \mathbf{u}_{l,h}) \cdot (\mathbf{u}_{l,\mathrm{exact}} - \mathbf{u}_{l,h})}{N}} \end{aligned} \tag{22}$$

being N the number of sampling points uniformly distributed over the domain (1600 for Test 1) and h is the mesh parameter, equal to the maximum diameter for FEM elements or to the maximum length for BEM elements.

The results obtained with the proposed technique are compared with the results obtained by using the Finite Element Method (FEM) with continuous quadratic basis functions implemented in COMSOL [56], and by using constant BEM elements and linear BEM elements. The four solutions are labeled in what follows BEM_Quad, FEM_Quad, BEM_Const and BEM_Linear, respectively.

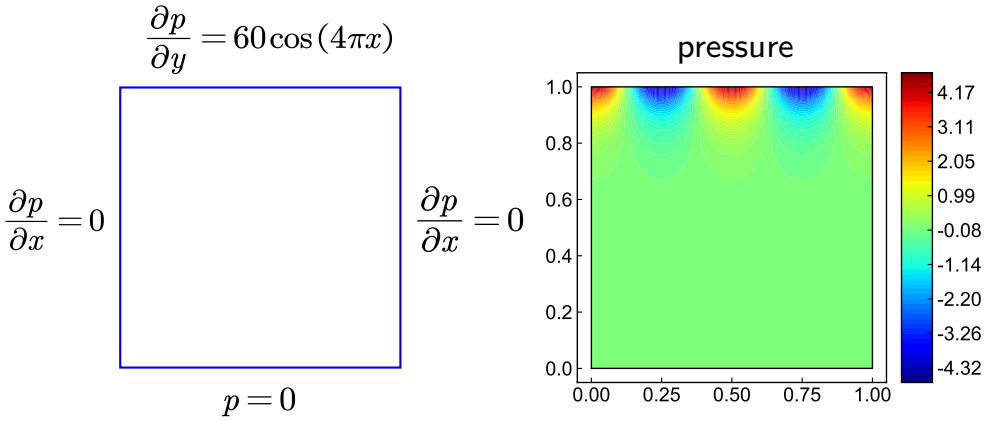

Figure 5: Test 1: a) boundary conditions; b) map of the pressure values for BEM_Quad

In Fig. 6 the convergence trends of the considered error indicators for the various methods are shown. Concerning the approximation of the pressure term, all the solutions exhibit expected optimal convergence rates, given the regularity of the solution and the polynomial accuracy of each method. In particular, it is observed that also the methods that use discontinuous basis functions are capable of providing extremely good approximations, and the approximation level of quadratic BEM is comparable to the one provided by quadratic FEM. Concerning the approximation of the velocity term, the proposed BEM technique has a superior convergence rate with respect to the FEM with basis functions of the same order. Also, this result is expected, since the derivative of p is directly computed with BEM, whereas, for the FEM solution, it is the result of post-processing from the FEM solution, that leads to a deterioration of the convergence results.

4.2. Test 2: unit square with 10 fractures

The second proposed example deals with a unit square fracture domain with 10 traces and one wellbore intersection (Fig. 7). In this example, several regions with sharp solution gradients are included, such as trace tips, intersections between traces, intersections between traces and fracture boundaries, or intersections between fractures and wellbores.

The proposed quadratic BEM technique is here validated comparing the BEM_Quad results with the results derived by using constant BEM elements (BEM_Const), and with the solution given by FEM with quadratic basis functions (FEM_Quad). Since the exact solution is not known in this case, an ad-

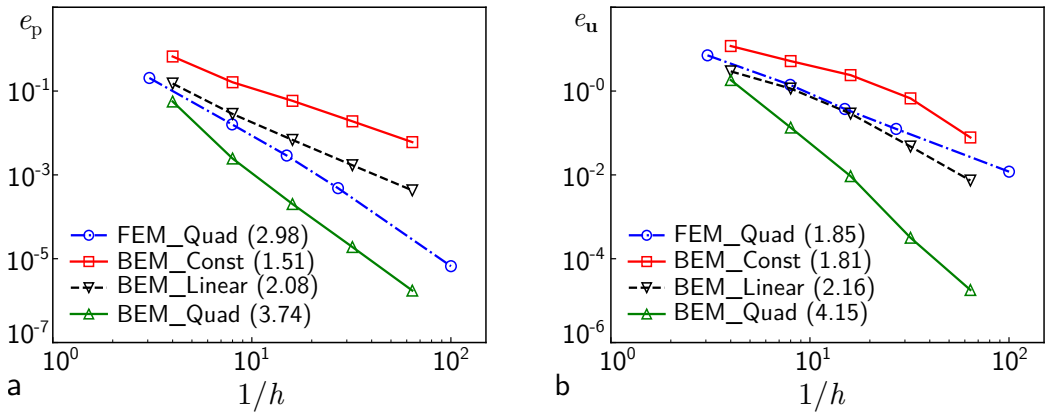

Figure 6: Test 1; Error indicators e_p (left) and $e_{\mathbf{u}}$ (right) plotted against the number of elements for FEM_Quad, BEM_Const, BEM_Linear, BEM_Quad methods; convergence rates in brackets

ditional solution is considered as a reference term, obtained using the FEM on a highly-refined mesh (FEM_Quad_Ref). Fluid viscosity is set to 2 Pa·s and fracture permeability is 3 m^2, whereas given pressure values are imposed on the traces and on the wellbore intersection, as detailed in Fig. 7. No flux conditions are instead set on the whole domain boundary.

In Fig. 8, the mesh setup for the three solutions are shown: a) the piece-wise constant BEM mesh, counting 348 elements and 348 DOFs; b) the quadratic BEM mesh, counting 116 quadratic elements and 346 DOFs; c) the FEM mesh, having 6887 elements and 13982 DOFs. Finally, the reference FEM mesh counts about 0.6 million elements and 1.2 million DOFs.

The shaded map of the pressure values from the BEM_Quad solution is reported in Fig. 7b; as expected, sharp gradients at trace tips and near the intersection with the well show. Two sampling lines, L1 and L2, in Fig. 7a are used for the comparison: L1 crosses several traces and intercepts the wellbore intersection, L2 is aligned along with one of the traces.

Results are presented in Figs. 9a,b, for pressure and velocity on L1 for x between 0 and 0.8, thus including trace tips and trace intersections. It can be observed that the proposed BEM technique with discontinuous quadratic basis functions is in excellent agreement with the reference solution, both for the pressures and the velocities. The BEM_Const solution is instead less accurate, near trace tips and trace intersections. In Figs. 9c,d, the pressure and velocity solutions near the wellbore intersection, for x between 0.8 and 1,

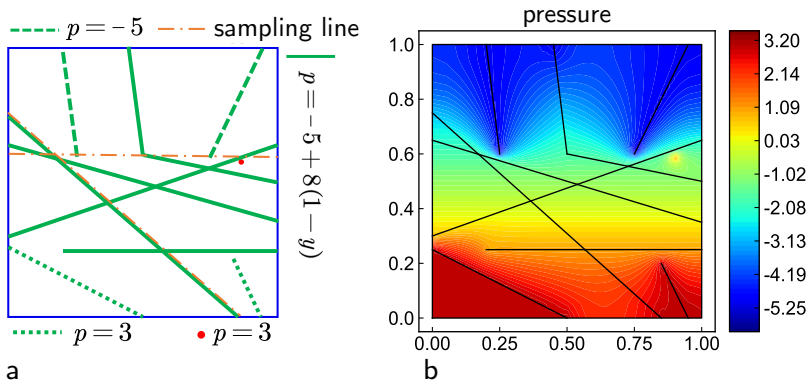

Figure 7: Scheme of Test 2: a) all edges of the unit square are subjected to an insulation (Neumann) boundary condition, prescribed pressures apply to all the traces and the wellbore; sampling lines for the inspection of pressures and velocities are dash-dotted; coordinates of the extremities (0.0,0.59)-(1.0, 0.59) for L1, and (0.0,0.75)-(0.85,0.0) for L2; b) map of the pressure values from the Quad_Bem solution

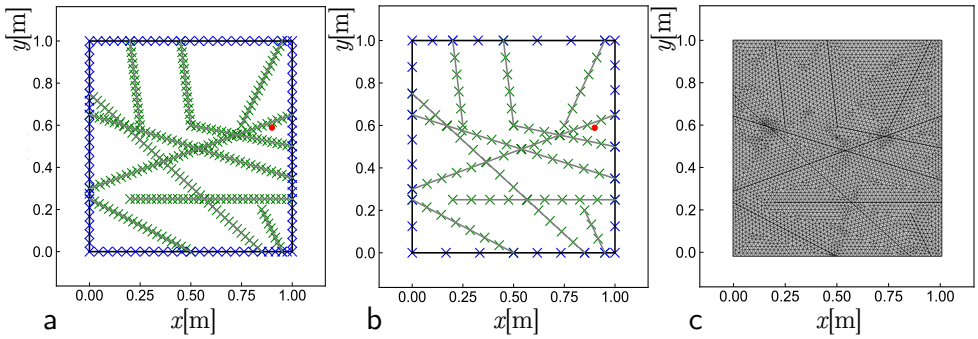

Figure 8: Meshes for Test 2: a) BEM mesh with constant elements (348 elements and 348 DOFs); b) BEM mesh with quadratic elements (116,346); c) FEM mesh with quadratic elements (6887,13982)

are shown. As expected, the FEM_Quad solution exhibits larger discrepancies from the reference solution for the velocities. Thanks to the exact point-source fundamental function adopted in BEM methods, instead, the two BEM-based solutions successfully capture the sharp pressure and velocity gradient in this region, by using only one DOF.

In Figs. 10a,b the line plots for the four solutions along L2 are reported. Also in this case the superior performance of the proposed BEM technique is apparent, displaying an excellent agreement with the reference solution. Both

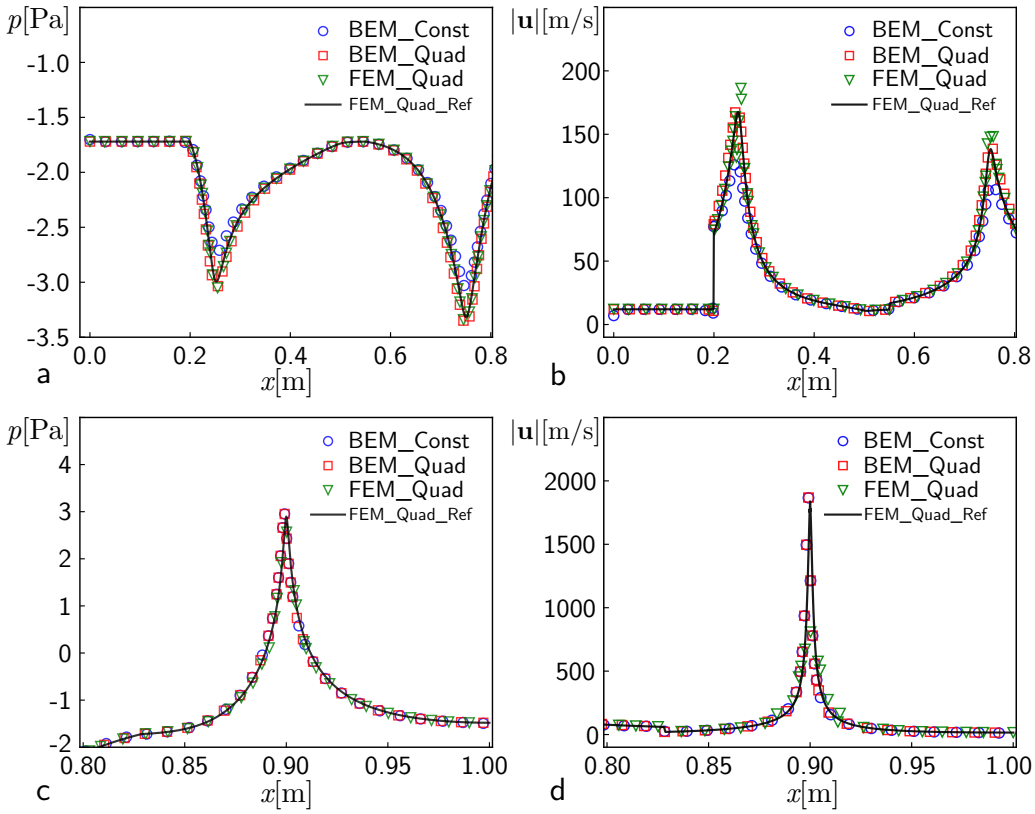

Figure 9: Test 2; Pressures and velocities at the points of sampling line L1; a-b: solutions for $0.0 \leq x \leq 0.8$,y=0.59; c-d: solutions for $0.8 \leq x \leq 1.0$,y=0.59

the FEM solution and the piece-wise constant BEM solution, instead, provide poorer approximations of the velocity solution near trace intersections and trace-edge intersections.

As far as the computational cost is concerned, the proposed BEM technique with quadratic element also shows advantages over the conventional FEM and BEM solutions for a given level of accuracy. It only uses 116 elements and 346 DOFs to obtain an excellent match with the highly refined reference solution.

4.3. Test 3: 4-fractures DFN

With reference to Fig. 11, the steady-state fluid flow in a small DFN consisting of four rectangular fractures is solved. The results of the proposed technique are compared with the results of a FEM model with quadratic ele-

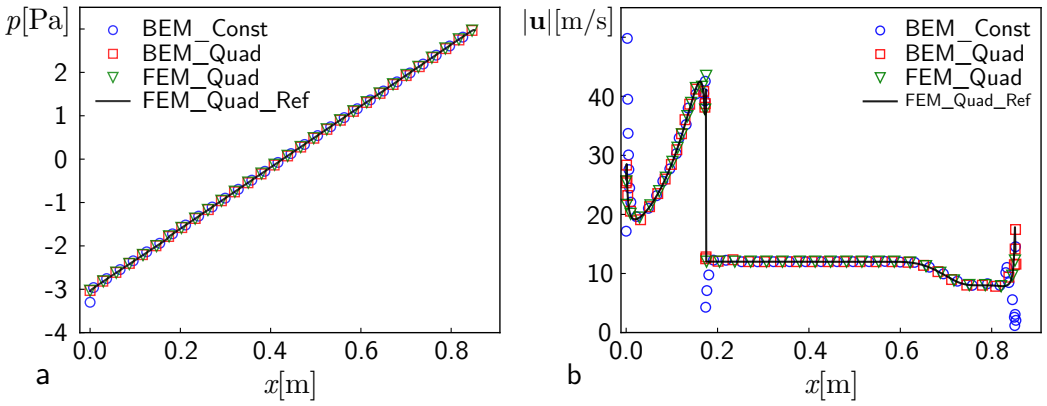

Figure 10: Test 2; Pressures (a) and velocities (b) at the points of sampling line L2

ments and a refined mesh (again solution FEM_Quad_Ref). Three horizontal fractures Ω_{2-4} intersect a vertical fracture Ω_1. The injection well s_{Inj} crosses Ω_3 and the production well s_{Pro} crosses two fractures, $\Omega_{2,4}$. Fixed pressure values for the injection well and production well are 2 MPa (p_{Inj}) and 1 MPa (p_{Pro}), respectively. The aperture values of the four fractures are 0.01 m. Wellbore radius is 0.001 m. The fluid viscosity and fracture permeability are 0.001 Pa $\cdot$ s and $3 \times 10^{-10}\text{m}^2$, respectively.

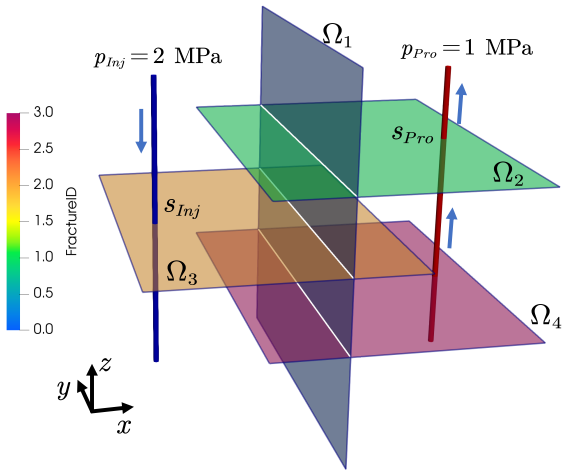

Figure 11: Test 3; the DFN is enclosed in a box $1\times1\times1\times\text{m}^3$, the wellbore radius is 0.001 m, the fracture apertures are constant and equal to 0.01m, injection S_{Inj} and production S_{Pro} wellbores are at pressures 2 MPa and 1 MPa, respectively

In Fig. 12, the pressure and velocity solutions of the presented BEM

technique are compared with the reference FEM solutions. For the BEM solution, only 87 boundary elements resulted sufficient to reach a perfect match with the FEM solution. The proposed BEM solution of this test case is obtained using the DDM algorithm 1, which allows solving, iteratively, small dense local linear systems instead of a large coupled unsymmetrical global system. The stopping tolerance TOL is set to 1×10^{-9} and the DDM algorithm converges in 112 iterations, providing a solution with maximum flux mismatch over all traces and wells equal to 4.2×10^{-9}. This error can be further minimized by reducing the stopping tolerance, with, however a minor impact on the global flux balance. The computed flux at the injection well is 13.03 m^3/day, in good agreement with the one provided by the reference FEM solution with 0.2 million elements (13.05 m^3/day, 0.2% difference). Also, the plots reported in Figs 12c,d along a line passing close to the injection well (the red line in Fig. 12a) are in very good agreement.

4.4. Test 4: 97-fractures DFN

The last example refers to a 97-fractures DFN (4 faults and 93 fractures) where there are 2 vertical wells, drilled through four faults (Fig. 13a). The 93 fractures are randomly generated by the open-source DFN modeling tool ADFNE [55]. Constant pressure values of 15 MPa and 10 MPa are fixed at the injection well and production well, respectively. No flow boundary conditions are prescribed on all fractures. Uniform aperture and permeability are assigned to all the fractures. Fracture aperture follows a log-normal distribution [21]. (Fig. 13b), with a mean value of -2.1 and a standard deviation value of 0.27 [57]). The cubic-law $k = {b_f}^2/12$ is then applied to calculate the corresponding values of fracture permeability [58]. The faults have an aperture of $3{\times}10^{-4}$m and a permeability of $7.5{\times}10^{-9}$m^2.

As a whole, 2146 discontinuous quadratic elements (23 elements per fracture plane) are used for this test. In Fig. 14a the BEM mesh for one of the faults of the DFN is shown; in Fig. 14b the steady-state pressure solution is reported. It is obtained with the DDM algorithm; 2132 iterations were required to reach a maximum flux balance error over all intersections and wells of 2.6×10^{-6} m^3/s. The performance of the parallel DDM algorithm in PyDFN3D could be easily accelerated through a parallel implementation in High Performance Computing (HPC) systems.

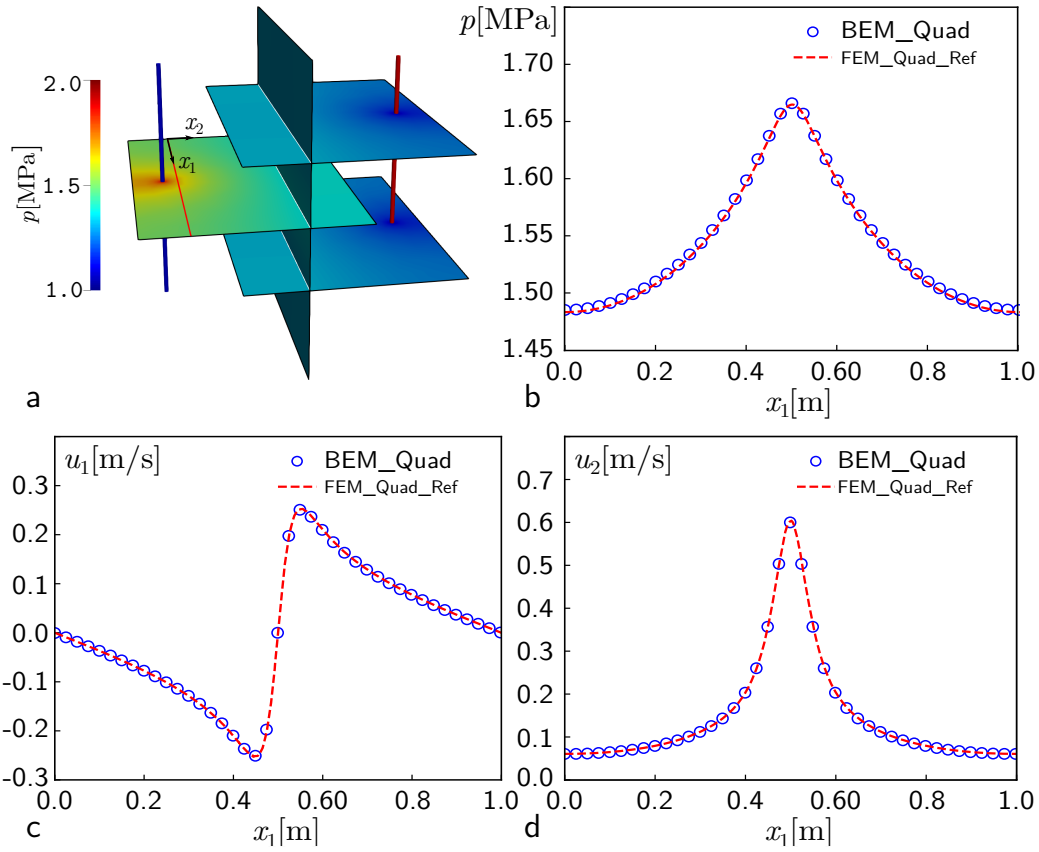

Figure 12: Quad_BEM solutions for Test 3: a) shading map of the pressures; pressure p (b), velocity component u_1 (c), velocity component u_2 (d) along the red sampling line in a, compared with the results obtained with FEM_Quad_Ref (x_1, x_2 local coordinates of the sampling line)

5. Conclusions

A novel numerical technique based on the Boundary Element Method (BEM) with discontinuous quadratic elements is presented and used in conjunction with a parallel domain decomposition method for the solution of steady-state fluid flow problems in 3D Discrete Fracture Networks (DFNs). Fast analytical integration formulations were derived to account for singular, nearly-singular and non-singular BEM integrals. Several examples were investigated to verify the accuracy and the applicability of the technique. The following conclusions can be drawn:

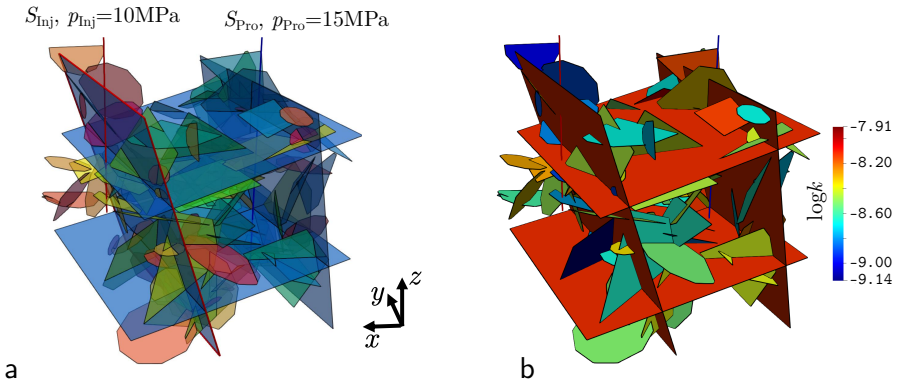

Figure 13: Test 4; a) DFN with 4 faults and 93 fractures, one injection well S_{Inj} and one production well S_{Pro} at pressures 15 MPa and 10 MPa, respectively; b) distribution of fracture permeability

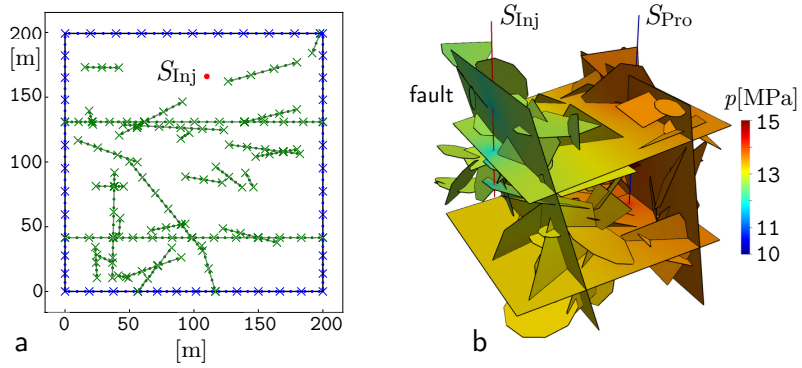

Figure 14: Test 4; a) BEM mesh of the fault; b) distribution of the computed pressures

- In the context of DFNs, with the proposed technique the limitations of previous BEM-based approaches with low order basis functions are overcome; in particular, better approximations near trace intersections and trace-boundary intersections are provided.
- Optimal convergence rates are achieved by the second-order discontinuous quadratic basis functions employed for the approximation of both pressure and velocity on fracture boundaries and traces;
- In the numerical examples an excellent agreement between the proposed method and a highly-refined reference FEM solution is gained;

- The use of the point source function results highly effective for the simulation of the sharp pressure gradients in the near-field of a wellbore;
- The technique can be effectively used in conjunction with DDM approaches, thus allowing for a possible parallel implementation pursuing computations speedup.

In future works, the convergence of the DDM algorithm could be improved, namely reducing the iteration count to reach a given tolerance. Also, the fracture-wise heterogeneities could be supported by adopting some advanced BEM methods, such as Dual Reciprocity BEM. This is useful for applications where the flow field is governed by few fractures with local heterogeneities.

Acknowledgments

This research was supported by Board of Regents of the State of Louisiana (LEQSF(2017-20)-RD-A-20). The authors express their appreciation to Dr. Boyun Guo (University of Louisiana at Lafayette) and Tianqi Ma (Fudan University) for their support. S.P. and S.S. acknowledge the support of INdAM-GNCS and acknowledge that the present research has been partially supported by MIUR grant Dipartimenti di Eccellenza 2018-2022 (E11G1800 0350001) and MIUR project PRIN 201744KLJL_004.

Appendix A. Derivation of the BIE

The governing equation for the fluid flow in a fracture is obtained in Eq. (4):

$$-\frac{kb_{\mathrm{f}}}{\mu}\nabla^2 p = \sum_{t\in T}\delta_{t,q_t} + \sum_{s\in S} q_s\delta_s \tag{A-1}$$

A weighted residual statement for Eq. (4) is as follows:

$$\begin{aligned} -\frac{kb_{\mathrm{f}}}{\mu}\left(\int_\Omega \nabla\cdot(\nabla p w)\mathrm{d}\Omega - \int_\Omega \nabla p\cdot\nabla w\mathrm{d}\Omega\right) \\ = \sum_{t\in T}\int_t q_t(\gamma)w(\gamma)d\gamma + \sum_{s\in S} q_s w\left(\mathbf{x}_s\right) \end{aligned} \tag{A-2}$$

where w is a weighting function. It can be re-written as follows:

$$\begin{aligned}\int_{\Omega} \nabla \cdot (w \nabla p) \mathrm{d}\Omega - \int_{\Omega} \nabla \cdot (p \nabla w) \mathrm{d}\Omega + \int_{\Omega} \nabla \cdot (\nabla w)\, p \mathrm{d}\Omega \\ = -\frac{\mu}{k b_{\mathrm{f}}} \left(\sum_{t \in T} \int_{t} q_t (\mathbf{x})\, w \mathrm{d}t + \sum_{s \in S} q_s w (\mathbf{x}_s) \right)\end{aligned} \tag{A-3}$$

By formally using twice the divergence theorem, once for $\int_{\Omega} \nabla \cdot (\nabla p w) d\Omega = \int_{\Gamma} w \nabla p \cdot \mathbf{n} d\Gamma$, and then $\int_{\Omega} \nabla \cdot (p \nabla w) d\Omega = \int_{\Gamma} p \nabla w \cdot \mathbf{n} d\Gamma$ one obtains:

$$\begin{aligned}\int_{\Gamma} w \nabla p \cdot \mathbf{n} \mathrm{d}\Gamma - \int_{\Gamma} p \nabla w \cdot \mathbf{n} \mathrm{d}\Gamma + \int_{\Omega} \nabla \cdot (\nabla w)\, p \mathrm{d}\Omega \\ = -\frac{\mu}{k b_{\mathrm{f}}} \left(\sum_{t \in T} \int_{t} q_t (\mathbf{x})\, w \mathrm{d}t + \sum_{s \in S} q_s w (\mathbf{x}_s) \right)\end{aligned} \tag{A-4}$$

which can be compactly rewritten as:

$$\begin{aligned}-\frac{k b_{\mathrm{f}}}{\mu} \left(\int_{\Gamma} w \frac{\partial p}{\partial \mathbf{n}} \mathrm{d}\Gamma - \int_{\Gamma} p \frac{\partial w}{\partial \mathbf{n}} \mathrm{d}\Gamma + \int_{\Omega} \nabla \cdot (\nabla w)\, p \mathrm{d}\Omega \right) \\ = \sum_{t \in T} \int_{t} q_t (\mathbf{x}) w \mathrm{d}t + \sum_{s \in S} q_s w (\mathbf{x}_s)\end{aligned} \tag{A-5}$$

If the weighting function w is assumed equal to the fundamental solution of Laplacian operator in 2D, say $w(\mathbf{x}, \mathbf{y})$, such that $\int_{\Omega} \nabla_{\mathbf{x}} \cdot (\nabla_{\mathbf{x}} w(\mathbf{x}, \mathbf{y}))\, d\mathbf{x} = \delta_{\mathbf{y}}$, then Eq (A-5) becomes:

$$\begin{aligned}-\frac{k b_{\mathrm{f}}}{\mu} \left(\int_{\Gamma} w \frac{\partial p}{\partial \mathbf{n}} \mathrm{d}\Gamma - \int_{\Gamma} p \frac{\partial w}{\partial \mathbf{n}} \mathrm{d}\Gamma - p \right) = \sum_{t \in T} \int_{t} q_t (\mathbf{x}) w dt \\ + \sum_{s \in S} q_s w (\mathbf{x}_s)\end{aligned} \tag{A-6}$$

The BIE is finally derived from Eq. (A-6) using the concept of half circle or half spherical problem [43] as:

$$\begin{aligned}-\frac{k b_{\mathrm{f}}}{\mu} \left(c (\mathbf{x}_i)\, p (\mathbf{x}_i) + \int_{\Gamma} p (\mathbf{x}) \frac{\partial w (\mathbf{x}_i, \mathbf{x})}{\partial \mathbf{n}} \mathrm{d}\Gamma \right) \\ = -\frac{k b_{\mathrm{f}}}{\mu} \int_{\Gamma} \frac{\partial p}{\partial \mathbf{n}} (\mathbf{x})\, w (\mathbf{x}_i, \mathbf{x})\, \mathrm{d}\Gamma - \sum_{t \in T} \int_{t} q_t (\mathbf{x})\, w (\mathbf{x}_i, \mathbf{x})\, \mathrm{d}t \\ - \sum_{s \in S} q_s w (\mathbf{x}_i, \mathbf{x}_s)\end{aligned} \tag{A-7}$$

where $\mathbf{x}_i$ denotes the source point, and $c(\mathbf{x}_i) = 1$ if $\mathbf{x}_i$ is located inside the domain or $c(\mathbf{x}_i) = \frac{1}{2}$ if $\mathbf{x}_i$ is located on the boundary, if the boundary is smooth [43].

Appendix B. Analytical integrations

By assuming that a quadratic BEM element is a straight line, as shown in Figs. [2-3], the integrals in Eq. (13) can be analytically calculated and the results of the integration subsequently reported in subsection 2.3 by using the integral quantities are reported in what follows.

The integrals depend on the locations of the two extreme nodes $(x_1(1), x_2(1))$ and $(x_1(3), x_2(3))$ of the integration element and of the collocation node (x_{1i}, x_{2i}). According to the method proposed by [49, 50], the following geometrical quantities are defined first:

$$\begin{aligned} D_1 &= \frac{x_1(3) - x_1(1)}{2}, \qquad D_2 = \frac{x_2(3) - x_2(1)}{2} \\ C_1 &= \frac{x_1(3) + x_1(1)}{2} - x_{1i}, \qquad C_2 = \frac{x_2(3) + x_2(1)}{2} - x_{2i} \\ a &= D_1^2 + D_2^2, \qquad b = 2\left(D_1 C_1 + D_2 C_2\right) \\ c &= C_1^2 + C_2^2, \qquad e = C_1 D_2 - C_2 D_1 \\ & \qquad\qquad J = L/2 \end{aligned} \tag{B-1}$$

where J is the Jacobian of the map from physical to reference space for a straight BE element having length L.

Using the constants defined above, the following integrals are solved:

$$\begin{aligned} F_n &= \int_{-1}^{1} \frac{\xi^n}{a\xi^2 + b\xi + c} \mathrm{d}\xi \\ A_n &= \int_{-1}^{1} \xi^n \ln\left(a\xi^2 + b\xi + c\right) \mathrm{d}\xi, \\ S_n &= \int_{-1}^{1} \xi^n \ln \frac{L}{2} \left|\xi - \xi_i\right| \mathrm{d}\xi \end{aligned} \tag{B-2}$$

With the help of the symbolic mathematics tool SymPy [59], the values of the above integrals can be found:

- Integrals F_n:

For $\sqrt{4ac-b^2}>0$:

$$F_0=\frac{2}{\sqrt{4ac-b^2}}\begin{pmatrix}\arctan\frac{2a+b}{\sqrt{4ac-b^2}}\\ -\arctan\frac{-2a+b}{\sqrt{4ac-b^2}}\end{pmatrix} \tag{B-3}$$

For $\sqrt{4ac-b^2}=0$:

$$F_0=\frac{2}{b-2a}-\frac{2}{b+2a} \tag{B-4}$$

$$\begin{aligned}
F_1&=\tfrac{1}{2a}\ln\tfrac{a+b+c}{a-b+c}-\tfrac{b}{2a}F_0, && \text{(B-5)}\\
F_2&=\tfrac{2}{a}-\tfrac{c}{a}F_0-\tfrac{b}{a}F_1 && \text{(B-6)}\\
F_3&=-\tfrac{c}{a}F_1-\tfrac{b}{a}F_2, && \text{(B-7)}\\
F_4&=\tfrac{2}{3a}-\tfrac{c}{a}F_2-\tfrac{b}{a}F_3, && \text{(B-8)}\\
F_5&=-\tfrac{c}{a}F_3-\tfrac{b}{a}F_4 && \text{(B-9)}
\end{aligned}$$

- Integrals A_n:

$$\begin{aligned}
A_0&=\ln\left[(a+c)^2-b^2\right]-2aF_2-bF_1,\\
A_1&=\frac{1}{2}\ln\frac{a+b+c}{a-b+c}-aF_3-\frac{1}{2}F_2,\\
A_2&=\frac{1}{3}\ln\left[(a+c)^2-b^2\right]-\frac{2}{3}aF_4-\frac{1}{3}bF_3
\end{aligned} \tag{B-10}$$

- Integrals S_n:

$$\begin{aligned}
S_0&=\ln\frac{L}{2}(1+\xi_i)+\ln\frac{L}{2}(1-\xi_i)-\xi_i\ln\frac{1+\xi_i}{1-\xi_i}-2\\
S_1&=\frac{1}{2}\left(1-\xi_i^2\right)\ln\frac{1+\xi_i}{1-\xi_i}-\xi_i\\
S_2&=(1+\xi_i)^3\left[\frac{1}{3}\ln\frac{L}{2}(1+\xi_i)-\frac{1}{9}\right]\\
&+(1-\xi_i)^3\left[\frac{1}{3}\ln\frac{L}{2}(1-\xi_i)-\frac{1}{9}\right]+2\xi_iS_1-\xi_i^2S_0
\end{aligned} \tag{B-11}$$

where ξ_i is the local coordinate of the collocation node when it lies on the integration element.

The following integrals are also computed:

$$G_n = \int_{-1}^{1} \frac{\xi^n}{\left(a\xi^2 + b\xi + c\right)^2} \mathrm{d}\xi, \quad T_n = \int_{-1}^{1} \frac{\xi^n}{|\xi - \xi_i|} \mathrm{d}\xi \tag{B-12}$$

In formula:

- Integrals G_n:
  For $\sqrt{4ac - b^2} > 0$:

$$G_1 = \frac{-2c + b}{\sqrt{4ac - b^2}\,(a + b + c)} - \frac{2c - b}{\sqrt{4ac - b^2}\,(a - b + c)} - \frac{b}{\sqrt{4ac - b^2}} F_0 \tag{B-13}$$

  For $\sqrt{4ac - b^2} = 0$:

$$G_1 = -\left[\frac{8a}{3\,(b - 2a)^3} + \frac{8a}{3\,(b + 2a)^3}\right] - \frac{2}{3}\left[\frac{1}{(2a + b)^2} - \frac{1}{(-2a + b)^2}\right] \tag{B-14}$$

$$G_2 = -\tfrac{1}{a(a-b+c)} - \tfrac{1}{a(a+b+c)} + \tfrac{c}{a} G_0 \tag{B-15}$$

$$G_3 = \tfrac{\ln \frac{a+b+c}{a-b+c} - 3abG_2 - \left(2ac+b^2\right)G_1 - bcG_0}{2a^2} \tag{B-16}$$

  where the quantity G_0 is as follows:
  For $\sqrt{4ac - b^2} > 0$:

$$G_0 = \frac{2a + b}{\sqrt{4ac - b^2}\,(a + b + c)} - \frac{-2a + b}{\sqrt{4ac - b^2}\,(a - b + c)} + \frac{2a}{\sqrt{4ac - b^2}} F_0 \tag{B-17}$$

  For $\sqrt{4ac - b^2} = 0$:

$$G_0 = \frac{8a}{3\,(b - 2a)^3} - \frac{8a}{3\,(b + 2a)^3} \tag{B-18}$$

- Integrals T_n:

$$T_0 = \ln \frac{1+\xi_i}{1-\xi_i}, \quad T_1 = \xi_i \ln \frac{1+\xi_i}{1-\xi_i} + 2, \\ T_2 = \xi_i^2 \ln \frac{1+\xi_i}{1-\xi_i} + 2\xi_i \tag{B-19}$$

Finally, the quantities E_{1n}, E_{2n} and I_{1n}, I_{2n} (n = 0,1,2) are defined as follows:

$$E_{1n} = C_1 F_n + D_1 F_{n+1}, \tag{B-20}$$

$$E_{2n} = C_2 F_n + D_2 F_{n+1}, \tag{B-21}$$

$$I_{1n} = 2e\,(C_1 G_n + D_1 G_{i+1}) - D_2 F_i, \tag{B-22}$$

$$I_{2n} = 2e\,(C_2 G_i + D_2 G_{i+1}) + D_1 F_i \tag{B-23}$$

References

[1] M. Iding, P. Ringrose, Evaluating the impact of fractures on the performance of the in salah co2 storage site, International Journal of Greenhouse Gas Control 4 (2010) 242–248.

[2] J. D. Hyman, S. Karra, N. Makedonska, C. W. Gable, S. L. Painter, H. S. Viswanathan, dfnworks: A discrete fracture network framework for modeling subsurface flow and transport, Computers & Geosciences 84 (2015) 10–19.

[3] K. Ostad-Ali-Askari, H. Ghorbanizadeh Kharazi, M. Shayannejad, M. J. Zareian, Effect of management strategies on reducing negative impacts of climate change on water resources of the isfahan–borkhar aquifer using modflow, River Research and Applications 35 (2019) 611–631.

[4] Z.-x. Sun, X. Zhang, Y. Xu, J. Yao, H.-x. Wang, S. Lv, Z.-l. Sun, Y. Huang, M.-y. Cai, X. Huang, Numerical simulation of the heat extraction in egs with thermal-hydraulic-mechanical coupling method based on discrete fractures model, Energy 120 (2017) 20–33.

[5] S. Karra, N. Makedonska, H. S. Viswanathan, S. L. Painter, J. D. Hyman, Effect of advective flow in fractures and matrix diffusion on natural gas production, Water Resources Research 51 (2015) 8646–8657.

[6] G. Zhang, Y. Zhang, A. Xu, Y. Li, Microflow effects on the hydraulic aperture of single rough fractures, Advances in Geo-Energy Research 3 (2019) 104–114.

[7] D. Ye, G. Liu, F. Gao, R. Xu, F. Yue, A multi-field coupling model of gas flow in fractured coal seam, Advances in Geo-Energy Research 5 (2021) 104–118.

[8] S. H. Lee, M. Lough, C. Jensen, Hierarchical modeling of flow in naturally fractured formations with multiple length scales, Water resources research 37 (2001) 443–455.

[9] M. Sahimi, Flow and transport in porous media and fractured rock: from classical methods to modern approaches, John Wiley & Sons, 2011.

[10] A. Fumagalli, E. Keilegavlen, S. Scialò, Conforming, non-conforming and non-matching discretization couplings in discrete fracture network simulations, Journal of Computational Physics 376 (2019) 694–712.

[11] J. D. Hyman, A. Hagberg, G. Srinivasan, J. Mohd-Yusof, H. Viswanathan, Predictions of first passage times in sparse discrete fracture networks using graph-based reductions, Physical Review E 96 (2017) 013304.

[12] S. Berrone, S. Scialò, F. Vicini, Parallel meshing, discretization, and computation of flow in massive discrete fracture networks, SIAM Journal on Scientific Computing 41 (2019) C317–C338.

[13] S. Berrone, C. Fidelibus, S. Pieraccini, S. Scialò, F. Vicini, Unsteady advection-diffusion simulations in complex discrete fracture networks with an optimization approach, Journal of Hydrology 566 (2018) 332–345. doi:10.1016/j.jhydrol.2018.09.031.

[14] S. Berrone, A. Borio, F. Vicini, Reliable a posteriori mesh adaptivity in discrete fracture network flow simulations, Computer Methods in Applied Mechanics and Engineering 354 (2019) 904–931.

[15] M. F. Benedetto, S. Berrone, S. Scialò, A globally conforming method for solving flow in discrete fracture networks using the virtual element method, Finite Elements in Analysis and Design 109 (2016) 23–36.

[16] A. Fumagalli, E. Keilegavlen, Dual virtual element method for discrete fractures networks, SIAM Journal on Scientific Computing 40 (2018) B228–B258.

[17] F. Dassi, A. Fumagalli, D. Losapio, S. Scialò, A. Scotti, G. Vacca, The mixed virtual element method on curved edges in two dimensions, Computer Methods in Applied Mechanics and Engineering 386 (2021) 114098.

[18] S. Berrone, A. Borio, A. D'Auria, S. Scialo, F. Vicini, A robust vem based approach for flow simulations in poro-fractured media, Mathematical Models and Methods in Applied Sciences (2021).

[19] P. F. Antonietti, L. Formaggia, A. Scotti, M. Verani, N. Verzott, Mimetic finite difference approximation of flows in fractured porous media, ESAIM: Mathematical Modelling and Numerical Analysis 50 (2016) 809–832.

[20] F. Chave, D. A. Di Pietro, L. Formaggia, A hybrid high-order method for darcy flows in fractured porous media, SIAM Journal on Scientific Computing 40 (2018) A1063–A1094.

[21] M.-C. Cacas, E. Ledoux, G. de Marsily, B. Tillie, A. Barbreau, E. Durand, B. Feuga, P. Peaudecerf, Modeling fracture flow with a stochastic discrete fracture network: calibration and validation: 1. the flow model, Water Resources Research 26 (1990) 479–489.

[22] W. Dershowitz, C. Fidelibus, Derivation of equivalent pipe network analogues for three-dimensional discrete fracture networks by the boundary element method, Water Resources Research 35 (1999) 2685–2691.

[23] C. Xu, C. Fidelibus, P. Dowd, Z. Wang, Z. Tian, An iterative procedure for the simulation of the steady-state fluid flow in rock fracture networks, Engineering geology 242 (2018) 160–168.

[24] N. Huang, R. Liu, Y. Jiang, Y. Cheng, Development and application of three-dimensional discrete fracture network modeling approach for fluid flow in fractured rock masses, Journal of Natural Gas Science and Engineering (2021) 103957.

[25] C. A. Andresen, A. Hansen, R. Le Goc, P. Davy, S. M. Hope, Topology of fracture networks, Frontiers in Physics 1 (2013) 7.

[26] J. D. Hyman, A. Hagberg, G. Srinivasan, J. Mohd-Yusof, H. Viswanathan, Predictions of first passage times in sparse discrete fracture networks using graph-based reductions, Physical Review E 96 (2017) 013304.

[27] S. Srinivasan, D. O'Malley, J. D. Hyman, S. Karra, H. S. Viswanathan, G. Srinivasan, Transient flow modeling in fractured media using graphs, Physical Review E 102 (2020) 052310.

[28] A. M. Shapiro, J. Andersson, Simulation of steady-state flow in three-dimensional fracture networks using the boundary-element method, Advances in water resources 8 (1985) 106–110.

[29] J. T. Katsikadelis, The boundary element method for engineers and scientists: theory and applications, Academic Press, 2016.

[30] B. Wang, Y. Feng, J. Du, Y. Wang, S. Wang, R. Yang, et al., An embedded grid-free approach for near-wellbore streamline simulation, SPE Journal 23 (2018) 567–588.

[31] A. M. Shapiro, J. Andersson, Steady state fluid response in fractured rock: a boundary element solution for a coupled, discrete fracture continuum model, Water Resources Research 19 (1983) 959–969.

[32] J. Andersson, B. Dverstorp, Conditional simulations of fluid flow in three-dimensional networks of discrete fractures, Water Resources Research 23 (1987) 1876–1886.

[33] V. Lenti, C. Fidelibus, A bem solution of steady-state flow problems in discrete fracture networks with minimization of core storage, Computers & geosciences 29 (2003) 1183–1190.

[34] R. Yang, Z. Huang, W. Yu, G. Li, W. Ren, L. Zuo, X. Tan, K. Sepehrnoori, S. Tian, M. Sheng, A comprehensive model for real gas transport in shale formations with complex non-planar fracture networks, Scientific reports 6 (2016) 36673.

[35] Z. Chen, X. Liao, X. Zhao, X. Dou, L. Zhu, Performance of horizontal wells with fracture networks in shale gas formation, Journal of Petroleum Science and Engineering 133 (2015) 646–664.

[36] Z. Chen, X. Liao, X. Zhao, L. Zhu, Influence of magnitude and permeability of fracture networks on behaviors of vertical shale gas wells by a free-simulator approach, Journal of Petroleum Science and Engineering 147 (2016) 261–272.

[37] Z. Chen, X. Liao, X. Zhao, X. Dou, L. Zhu, L. Sanbo, et al., A finite-conductivity horizontal-well model for pressure-transient analysis in multiple-fractured horizontal wells, SPE Journal 22 (2017) 1–112.

[38] Z. Chen, X. Liao, K. Sepehrnoori, W. Yu, et al., A semianalytical model for pressure-transient analysis of fractured wells in unconventional plays with arbitrarily distributed discrete fractures, SPE Journal (2018).

[39] B. Dverstorp, J. Andersson, Application of the discrete fracture network concept with field data: Possibilities of model calibration and validation, Water Resources Research 25 (1989) 540–550.

[40] L. Smeraglia, M. Mercuri, S. Tavani, A. Pignalosa, M. Kettermann, A. Billi, E. Carminati, 3d discrete fracture network (dfn) models of damage zone fluid corridors within a reservoir-scale normal fault in carbonates: Multiscale approach using field data and uav imagery, Marine and Petroleum Geology 126 (2021) 104902.

[41] Z. Chen, Reservoir simulation: mathematical techniques in oil recovery, volume 77, Siam, 2007.

[42] Y. Dong, Y. Fu, T.-C. J. Yeh, Y.-L. Wang, Y. Zha, L. Wang, Y. Hao, Equivalence of discrete fracture network and porous media models by hydraulic tomography, Water Resources Research 55 (2019) 3234–3247.

[43] C. A. Brebbia, J. Dominguez, Boundary elements: an introductory course, WIT press, 1994.

[44] M. Fratantonio, J. Rencis, Exact boundary element integrations for two-dimensional laplace equation, Engineering Analysis with Boundary Elements 24 (2000) 325–342.

[45] K. Aziz, A general single-phase wellbore/reservoir coupling model for multilateral wells, SPE Reservoir Evaluation & Engineering 4 (2001) 327–335.

[46] Y. Liu, N. Nishimura, The fast multipole boundary element method for potential problems: a tutorial, Engineering Analysis with Boundary Elements 30 (2006) 371–381.

[47] M. Tanaka, V. Sladek, J. Sladek, Regularization techniques applied to boundary element methods, Applied Mechanics Reviews 47 (1994) 457–499.

[48] Y. Gu, Q. Hua, W. Chen, C. Zhang, Numerical evaluation of nearly hyper-singular integrals in the boundary element analysis, Computers & Structures 167 (2016) 15–23.

[49] X. Zhang, X. Zhang, Exact integration in the boundary element method for two-dimensional elastostatic problems, Engineering analysis with boundary elements 27 (2003) 987–997.

[50] X. Zhang, X. An, Exact integration and its application in adaptive boundary element analysis of two-dimensional potential problems, Communications in Numerical Methods in Engineering 24 (2008) 1239–1250.

[51] S. Berrone, S. Pieraccini, S. Scialò, A pde-constrained optimization formulation for discrete fracture network flows, SIAM Journal on Scientific Computing 35 (2013) B487–B510.

[52] S. Berrone, S. Pieraccini, S. Scialò, An optimization approach for large scale simulations of discrete fracture network flows, Journal of Computational Physics 256 (2014) 838–853.

[53] S. Berrone, S. Pieraccini, S. Scialò, F. Vicini, A parallel solver for large scale dfn flow simulations, SIAM Journal on Scientific Computing 37 (2015) C285–C306.

[54] B. Wang, Y. Feng, S. Pieraccini, S. Scialò, C. Fidelibus, Iterative coupling algorithms for large multidomain problems with the boundary element method, International Journal for Numerical Methods in Engineering 117 (2019) 1–14.

[55] Y. F. Alghalandis, Adfne: Open source software for discrete fracture network engineering, two and three dimensional applications, Computers & Geosciences 102 (2017) 1–11.

[56] COMSOL Inc, Multiphysics reference guide for comsol 5.2, 2019. URL: `https://www.comsol.com/`.

[57] D. T. Snow, The frequency and apertures of fractures in rock, in: International journal of Rock mechanics and Mining sciences & Geomechanics Abstracts, volume 7, Elsevier, 1970, pp. 23–40.

[58] R. W. Zimmerman, G. S. Bodvarsson, Hydraulic conductivity of rock fractures, Transport in porous media 23 (1996) 1–30.

[59] A. Meurer, C. P. Smith, M. Paprocki, O. Čertík, S. B. Kirpichev, M. Rocklin, A. Kumar, S. Ivanov, J. K. Moore, S. Singh, et al., Sympy: symbolic computing in python, PeerJ Computer Science 3 (2017) e103.